

# Controlled Sixfold Symmetric Exfoliation of Oriented MoS<sub>2</sub> Monolayers by Coulomb Force

Sheng Liu,\* Chee Fai Fong, Xue Liu, Beng Hau Tan, Qingyun Zeng, Yoshinori Okada, Nam-Trung Nguyen, and Hongjie An\*

Atoms, molecules, and nanoparticles can be spatially manipulated by an atomic force microscopy (AFM) tip, through van der Waals (vdW) and/or Coulomb forces. These point-to-point manipulations are highly accurate at nanoscale, facilitating the construction and modification of nanostructures. Nevertheless, it is difficult to manipulate 2D layers in vdW crystals by an AFM tip, because the tip-induced attractive force is usually insufficient to outcompete the interlaminar vdW forces. Herein, manipulation of the surface layers on a MoS<sub>2</sub> single crystal by a conductive AFM tip is successfully reported. By applying a bias between the tip and MoS<sub>2</sub>, the Coulomb attractive force allows the topmost MoS<sub>2</sub> layers to be picked up. These exfoliated layers are deformed into micron-sized bubbles with sixfold symmetry, which are composed of high-quality monolayers and visually reflecting the hexagonal lattice orientation. The underlying mechanisms of the sixfold symmetric exfoliation and the formation of monolayers are discussed by in situ monitoring of the tunneling volt-ampere characteristics and simulation of the force distribution. The findings open a new route to obtain high-quality transition metal dichalcogenide (TMD) monolayers and their derived nanostructures on the surface of TMD single crystals for optoelectronic and photonic device applications.

## 1. Introduction

The Group VIB transition metal dichalcogenides (TMDs) exhibit indirect-to-direct band gap transition when thinning down to monolayers.<sup>[1,2]</sup> The TMD Monolayers show remarkable properties including room temperature robust excitons with binding energy up to  $\approx 200$  meV,<sup>[3–6]</sup> nonlinear optical susceptibility,<sup>[7–9]</sup> and valley polarization.<sup>[10–13]</sup> Recently, the stacking of monolayer and/or multilayers with a relative angle of homo- and hetero- TMDs has also led to the burgeoning field of twistronics.<sup>[14–16]</sup> The optoelectronic and valleytronic properties of TMD monolayers and heterostructures are highly related to the in-plane orientation of their hexagonal lattice.<sup>[6–8,10–12,14–18]</sup> To date, most of the frontier research works in this field are realized using the mechanically exfoliated monolayers, owing to the high crystalline quality of the master single crystals. Unfortunately, the exfoliation

S. Liu, Y. Okada  
 Quantum Materials Science Unit  
 Okinawa Institute of Science and Technology Graduate University  
 Okinawa 904-0495, Japan  
 E-mail: [sunnearby@hotmail.com](mailto:sunnearby@hotmail.com)

C. F. Fong  
 Nanoscale Quantum Photonics Laboratory  
 RIKEN Cluster for Pioneering Research  
 Saitama 351-0198, Japan

C. F. Fong  
 Quantum Optoelectronics Research Team  
 RIKEN Center for Advanced Photonics  
 Saitama 351-0198, Japan

 The ORCID identification number(s) for the author(s) of this article can be found under <https://doi.org/10.1002/admi.202300580>

© 2024 The Authors. Advanced Materials Interfaces published by Wiley-VCH GmbH. This is an open access article under the terms of the [Creative Commons Attribution](https://creativecommons.org/licenses/by/4.0/) License, which permits use, distribution and reproduction in any medium, provided the original work is properly cited.

DOI: 10.1002/admi.202300580

X. Liu  
 Key Laboratory of Structure and Functional Regulation of Hybrid Materials of Ministry of Education  
 Institutes of Physical Science and Information Technology, Anhui University  
 Hefei 230601, China

B. H. Tan  
 Low Energy Electronic Systems  
 Singapore-MIT Alliance for Research and Technology  
 Singapore 138602, Singapore

Q. Zeng  
 College of Shipbuilding Engineering  
 Harbin Engineering University  
 Harbin 150001, China

N.-T. Nguyen, H. An  
 Queensland Micro and Nanotechnology Centre  
 Griffith University  
 170 Kessels Road, Nathan, Queensland 4111, Australia  
 E-mail: [hongjie.an@griffith.edu.au](mailto:hongjie.an@griffith.edu.au)

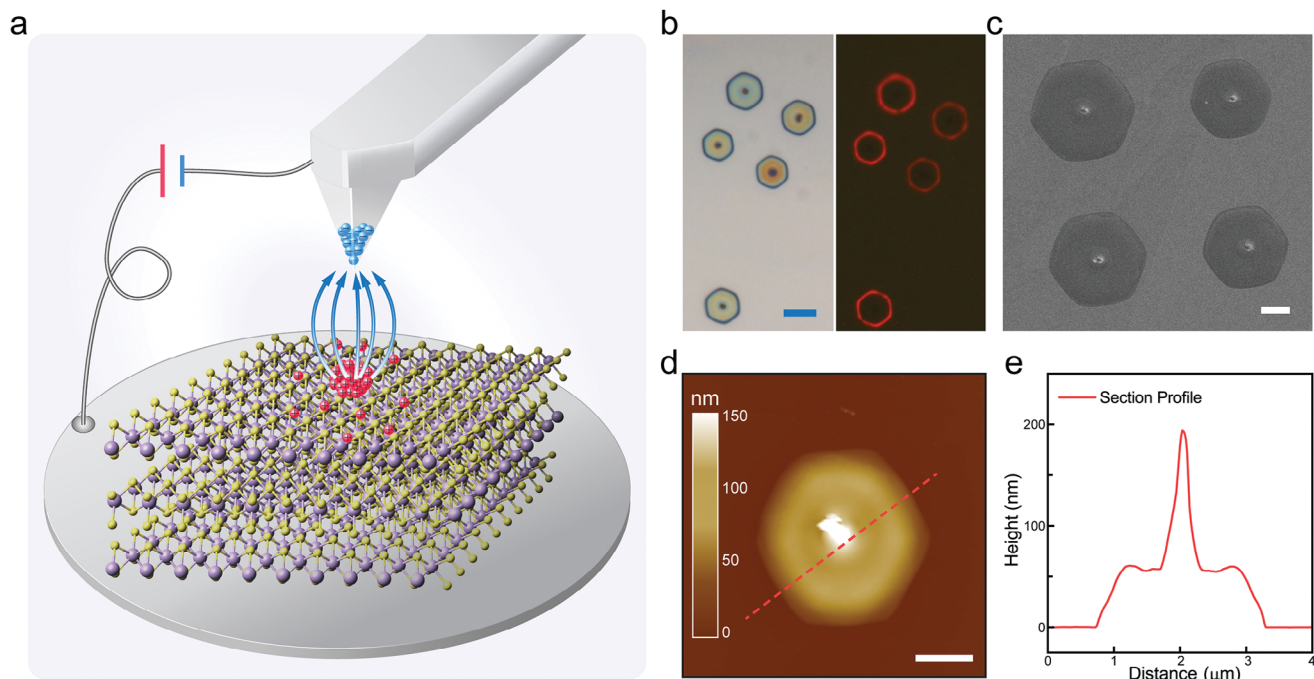


**Figure 1.** Illustration of the electrostatic force induced hexagonal bubble on MoS<sub>2</sub> single crystal surface using conductive AFM tip. a) illustration of the electrostatic field between the AFM tip and MoS<sub>2</sub> surface, the red and blue dot denote positive and negative charges, respectively; b) optical microscopic and fluorescent images of the hexagonal bubbles (scale bar: 5 μm); c) SEM image of the hexagonal bubbles (scale bar: 2.5 μm); d) AFM topography of a typical hexagonal bubble (scale bar: 1 μm); e) section profile of (d) along the red dashed line.

process is uncontrollable, where the monolayers come out one in thousands of flakes with random layer numbers and orientations, leaving the expansive surface area (ranging from millimeters to centimeters) on single crystals wasted.

The surface of TMD single crystals contain high-quality and highly oriented vdW layers. If one can manipulate and decouple those surface layers locally and precisely, it will open up an effective way to create high-quality TMD monolayers. Atomic force microscopy (AFM) is a versatile tool in modern nanotechnology. It can efficiently measure surface morphology, force (modulus) and potential at nanoscale both laterally and vertically.<sup>[19–21]</sup> Besides structural measurement, using the AFM tip to spatially manipulate atoms, molecules and nanoparticles is another essential application.<sup>[22–26]</sup> A typical AFM tip has tip radius in the scale around tens of nanometers or even smaller. Such small area provides a nanoscale “tweezer” to catch nano-objects with sizable attractive van der Waals (vdW) force. There are nonetheless many cases when the vdW force is insufficient to accomplish those nano manipulations, then Coulomb attractive force can be adopted as a supplement, by using conductive AFM tip and applying bias voltage between the tip and the target nano-objects.<sup>[27,28]</sup> It is worth noting that metal-assisted (especially Au-assisted) exfoliation can yield large-area monolayer TMDs with lateral size up to hundreds of micrometers or even millimeters,<sup>[29–31]</sup> owing to the large binding energy and covalent nature of the S/X or Se/X interfaces (X = Au, Ag, Pt, Cu, Ni etc.). Similarly, a conductive AFM tip coated with Pt or Au is likely to enhance the manipulation of the TMD surface.

In the article, we report a successful manipulation of the surface layers on MoS<sub>2</sub> single crystal using conductive AFM tip. By applying 2–10 V positive bias voltages to the MoS<sub>2</sub> crystal, surface layers are picked up locally by the Coulomb attractive force from the tip proximate to the MoS<sub>2</sub> surface at a distance within tens of nanometers. Those raised surface layers deform into microbubbles with hexagonal shape. Under Photoluminescence (PL), time-resolved photoluminescence (TRPL) and second harmonic generation (SHG) spectroscopic examinations, the lateral edge of the hexagonal bubbles are composed of high-quality MoS<sub>2</sub> monolayers, and their hexagonal shapes match seamlessly with the lattice orientation of the MoS<sub>2</sub> crystal. By in situ monitoring the tunnelling volt-ampere characteristics to the AFM tip, the formation mechanism of the hexagonal bubbles and the edge monolayers are well resolved. The surface layers on MoS<sub>2</sub> crystal are manipulated by the AFM tip through the bias-enhanced Coulomb force, while the bubble formation follows the sixfold symmetry of the MoS<sub>2</sub> crystal lattice. Our results introduce an effective way to precisely construct nanostructures and valleytronic photon emitters on the surface of TMDs.

## 2. Results

### 2.1. Manipulating the Surface Layers on MoS<sub>2</sub> with a Conductive AFM Tip

The surface layers of a 2H-MoS<sub>2</sub> single crystal is manipulated using a conductive AFM tip (coated with Pt/Ir), as shown schematically in Figure 1a. Details of the sample preparation and

mounting are described in the Experimental Section and Section S1 (Supporting Information). The AFM tip is set at constant distance (20–40 nm) proximate to the surface of MoS<sub>2</sub> sample, with a positive bias voltage (2–10 V) applied to the sample simultaneously. In this scenario, positive and negative charges (red and blue spheres in Figure 1a) accumulate locally at the approximate area, inducing electric polarization and Coulomb attraction between the sample surface and the AFM tip, causing hexagon shaped bubbles to form on the MoS<sub>2</sub> surface (a video showing the formation process is provided as Supporting Information). Figure 1b shows an optical microscopic image (left panel) of those hexagonal bubbles (HBs) and the corresponding fluorescent image (right panel). Glowing red hexagonal rings are observed in the fluorescent image, showing that the lateral edge of the HBs is highly radiative, while the main body of the HBs and the surrounding bulk MoS<sub>2</sub> surface exhibit negligible emission.

The morphology of the MoS<sub>2</sub> HBs is further examined by scanning electron microscope (SEM) and AFM. The SEM (Figure 1c) and AFM (Figure 1d) images of the HBs show sharp lateral edge of hexagonal geometry, consistent with the optical microscopic images. The AFM topography (Figure 1d) illustrates the stereoscopic structure of a typical HB, which is bulged up from the MoS<sub>2</sub> surface. The section profile of the bubble along the red dashed line in Figure 1d is plotted in Figure 1e. The HB has a two-part configuration, including a cone and an underlying hexagon base. The lateral and vertical sizes of the HBs are typically around 3–6 μm and 100–300 nm, respectively, depending on setting parameters of the AFM operation, which will be discussed in latter parts of the article.

## 2.2. Optical Properties of the Hexagonal Bubbles

The HB edge emits strong photoluminescence, which is one of the signatures of the direct bandgap monolayer MoS<sub>2</sub>. We further investigate the optical properties of the HBs by measuring the SHG, PL, time- and polarization-resolved PL. Figure 2a is a false-color map of SHG intensity of a typical HB, showing significant SHG signal at its hexagonal edge, similar to the fluorescent image. The SHG spectra taken at the HB edge (red), center (blue), and surrounding bulk MoS<sub>2</sub> area (black) are plotted in Figure 2b for comparison. The HB edge presents intense SHG peak at 400 nm, which is attributed to frequency doubling of excitation laser at 800 nm. In stark contrast, the HB center and bulk MoS<sub>2</sub> show no SHG signal. Theoretical and experimental results demonstrate that SHG susceptibility  $\chi^{(2)}$  is only valid in MoS<sub>2</sub> of odd layer number which has noncentrosymmetric lattice structure (Figure S2, Supporting Information).<sup>[7,9,32–34]</sup> The co-existing SHG and PL intensity unambiguously demonstrates that the HB edge is composed of monolayer MoS<sub>2</sub>.

In addition to the SHG map, angle-resolved SHG is measured at arbitrary spots on the HB edge, and the SHG intensities are shown as a polar plot (Figure 2c). The polar pattern demonstrates a sixfold symmetry, which is consistent with previous results of TMDs monolayers.<sup>[7–9,34]</sup> Interestingly, the hexagonal geometric orientations of the sixfold SHG pattern and the HB match well with each other. For monolayer TMDs, it has been known that those lobes of the polar pattern are aligned to the directions of Mo-S bonds, as they provide the strongest electric polarization

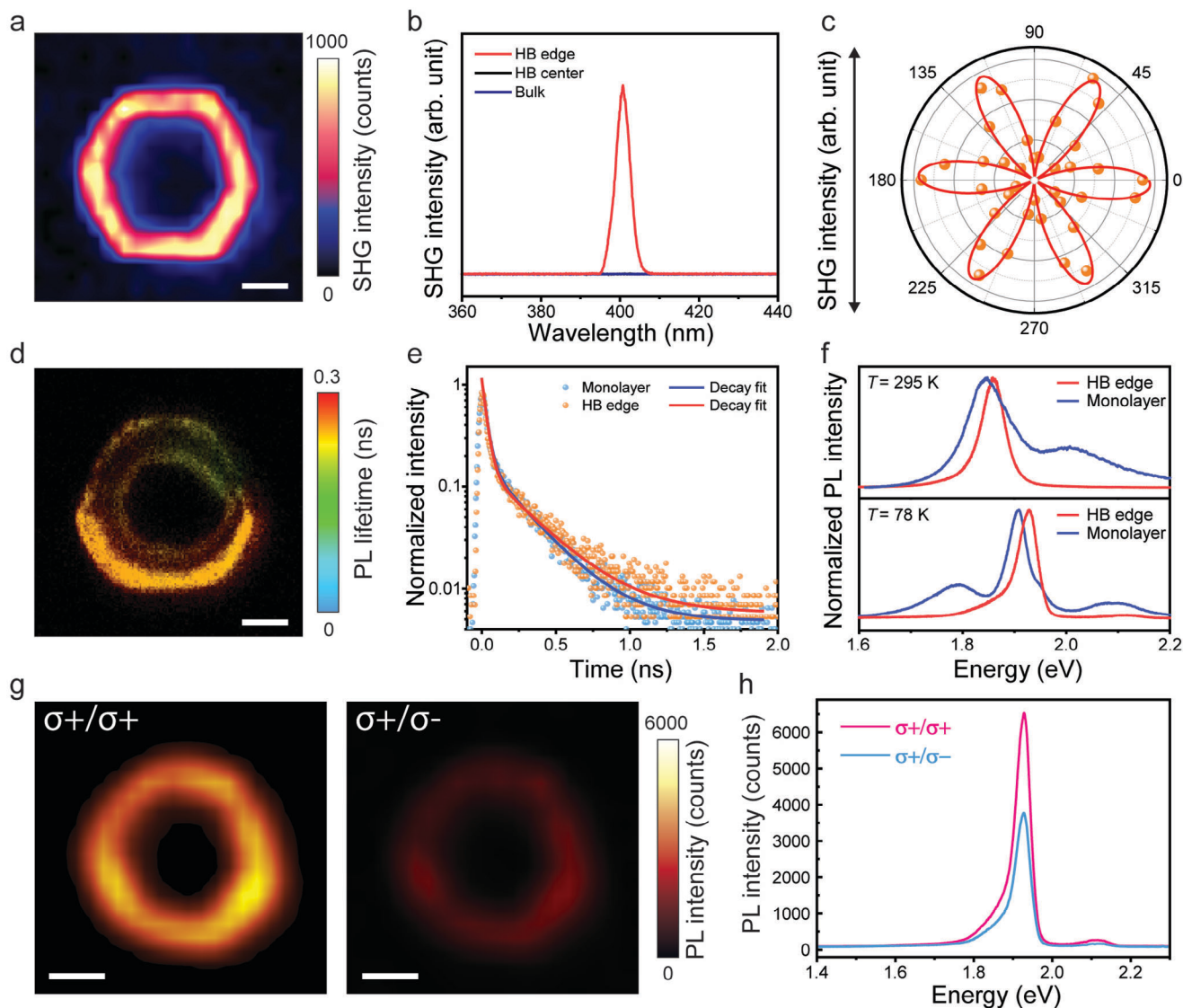
and  $\chi^{(2)}$  tensor within the basal plane of the 2D crystal.<sup>[7,8,35,36]</sup> As a result, the HBs on a MoS<sub>2</sub> surface share the same hexagon shape and orientation, which are identical to the lattice orientation of the MoS<sub>2</sub> single crystal.

Figure 2d shows a false-color map of the average PL lifetime taken on a typical HB. The PL emission from the HB edge displays a lifetime within 300 picoseconds homogeneously. An accumulative TRPL spectrum from the map is plotted in Figure 2e (red), together with a spectrum taken on the reference sample of exfoliated monolayer MoS<sub>2</sub> (blue) with their respective PL intensities normalized to their maxima. The two TRPL spectra match well with each other, both showing bi-exponential time decay curves with one ultra-fast and another longer decay. The results are in agreement to the typical excitonic recombination dynamics of monolayer MoS<sub>2</sub> reported in previous literature.<sup>[6,12,37,38]</sup>

Figure 2f shows the PL spectra of the HB edge (red) and the on-substrate exfoliated monolayer MoS<sub>2</sub> (blue) at room temperature and 78 K. The PL spectra of the HB edge present trion, A and B exciton peaks, similar to the on-substrate monolayer. The A exciton on HB edge has much stronger PL intensity comparing to on-substrate monolayers, making the PL intensity of the B exciton looks weaker. At both room temperature and 78 K, the HB edge has prominently narrower linewidths of the emission peaks, suggesting high crystalline quality. The line shape of neutral exciton (X) and trion (X<sup>-</sup>) peaks of A excitonic level can be well resolved at 78 K, clearly showing that the neutral exciton dominates the spectrum of the HB edge. By tracing the temperature-dependence of the exciton and trion peaks (Section 2, Supporting Information), we further confirm that the trion population in the HB edge is greatly suppressed, which makes the integrated linewidth narrower. It is also worth noting that the broad band emission at lower energy side of A exciton, which is attributed to defects and localized states,<sup>[39,40]</sup> is absent in the PL spectra of the HB edge. It highlights the high crystalline quality of the monolayers in the HB edge. Therefore, valley polarization is observed not surprisingly, as shown in the circularly polarized PL map (Figure 2g) and spectra (Figure 2h).

## 2.3. Fermi Energy and Inner Structure of the Hexagonal Bubbles

In light of the dominant neutral exciton population, the Fermi energy of the HB edge must have been dramatically modified, compared to conventional on-substrate monolayer MoS<sub>2</sub> which is a well-accepted *n*-type semiconductor.<sup>[12,41–43]</sup> To evaluate the charge density and electrostatic properties of the HBs, surface Kelvin potential microscopy (SKPM) was performed, with the potential map shown in Figure 3a. A positive potential of ≈40 mV is detected globally on the HB area, compared to the surrounding bulk MoS<sub>2</sub> surface, indicating that the HB area generally hosts less population of resident charge. The results match well with the suppression of trion population derived from the trion peak intensity in PL spectra (Section S2, Supporting Information), demonstrating that the MoS<sub>2</sub> monolayers at HB edge are more *p*-type like comparing to the on-substrate monolayer. Previous studies have verified that the surface potential and work function of on-substrate MoS<sub>2</sub> decrease and increase respectively with increasing the sample thickness (layer number).<sup>[44–46]</sup> In our observations, the HB area shows 40 mV



**Figure 2.** Optical properties of the HB edge showing its monolayer essence. a) 2D map of second-harmonic generation intensity on a typical HB (scale bar: 1.5  $\mu\text{m}$ ); b) second-harmonic generation spectra taken on the HB edge, center and bulk MoS<sub>2</sub> crystal; c) polar plot of second-harmonic generation intensity of the HB edge showing the polarization pattern; d) 2D map of the fluorescence lifetime of the HB edge (scale bar: 1.5  $\mu\text{m}$ ); e) PL decay spectra of the HB edge (orange trace) and monolayer MoS<sub>2</sub> on SiO<sub>2</sub>/Si substrate (cyan trace), whose exponential fittings are shown as red and blue lines respectively; f) PL spectra of the HB edge (red line) and monolayer MoS<sub>2</sub> on substrate (blue line) at room temperature and 78 K; circularly-polarized PL map (g) taken at a HB area (scale bar: 2  $\mu\text{m}$ ) and the extracted spectra (h).  $\sigma^+/\sigma^+$  and  $\sigma^+/\sigma^-$  denote left-hand and right-hand circular polarization at detection (excitation laser is left-hand circularly polarized).

higher surface potential (lower work function) compared to the surrounding bulk MoS<sub>2</sub>. The results suggest that the MoS<sub>2</sub> in HB area is thinner than the surrounding, in agreement with our spectroscopic demonstration of exfoliated monolayer in HB edge area. During the HB formation, local MoS<sub>2</sub> surface proximate to the tip is positively polarized, which also raises the surface potential and creates a gradient of the potential. After the applied voltage is removed, the potential gradient crossing the HB body will be evened, while the potential difference across the HB edge can be preserved because of the energy barrier induced by bandgap offset between the HB edge and the surrounding bulk MoS<sub>2</sub> (see Figure S5, Supporting Information). As a

result, the higher surface potential in HB area have multiple origins combining electrostatic and layer-dependence effects. It is worth noting that some recent studies demonstrate that the electrostatic potential of TMD monolayers modulate their optoelectronic and valleytronic properties,<sup>[6,12,17,18]</sup> as prominently as layer-dependence does.

A force mapping is taken on the HB area by scanning the AFM tip in a 20  $\times$  20 matrix and making nanoindentation at each stop. The on-site Young's modulus can be extracted (see details at Section S3, Supporting Information), making up a 2D contour as shown in Figure 3b. The Young's modulus of the HB is around 0.35–0.57 GPa (black region), which is irrationally lower than the

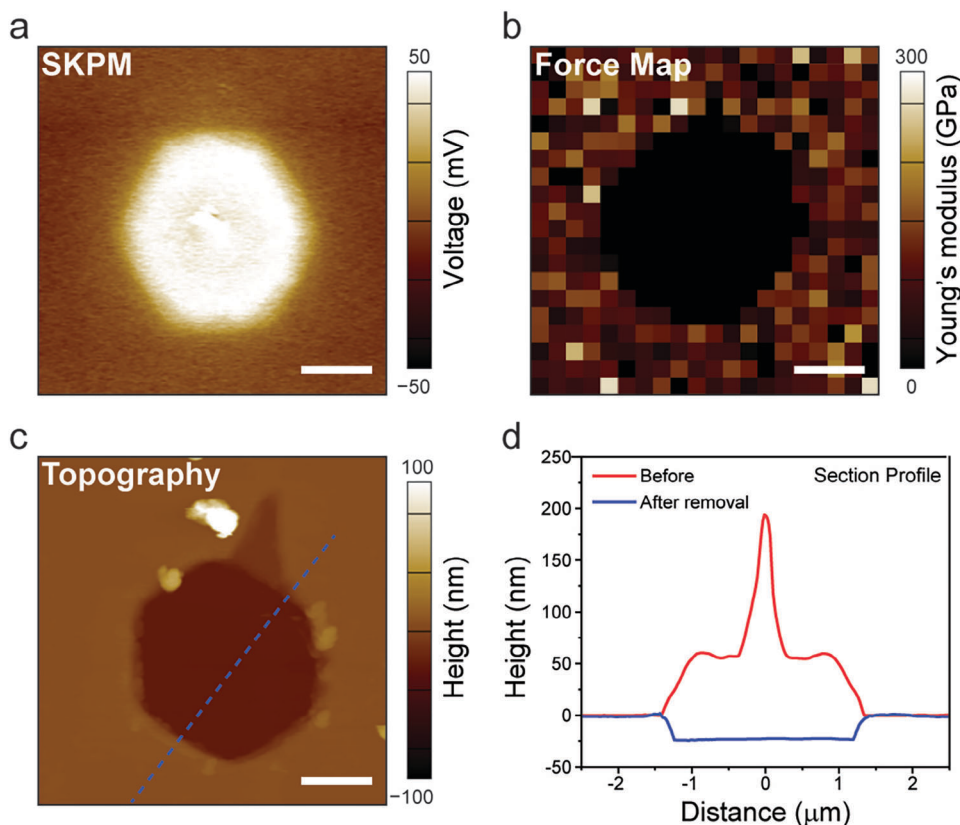


**Figure 3.** Surface potential and inner structure of the MoS<sub>2</sub> hexagonal bubbles. The scale bars represent 1 μm. a) surface potential map of a typical HB measured by SKPM; b) force mapping showing Young's modulus around the HB area. The Young's modulus is calculated from each force curve by Sneddon (conical) model; c) AFM topography after the bubble has been mechanically destroyed and removed by scanning with contact mode, showing the left hexagonal pit; d) section profiles from Figure 1d,e (red line) and (c) (blue line), the height of bubble and the depth of the hexagonal pit are ≈62 and 23 nm.

surrounding bulk MoS<sub>2</sub> (240–350 GPa). To unveil the inner structure, we shear off the HB shell by scanning the MoS<sub>2</sub> surface in AFM contact mode with feedback off. In this manner, the compelling force at tip/surface is high enough to slice off the raised MoS<sub>2</sub> layers when the tip reaches the HB edge. Figure 3c shows the topography of the HB area after removing the shell. A hexagonal pit appears, with sharp lateral edge and smooth bottom surface. As shown in Figure 3d, by aligning the section profiles of the hexagonal pit (blue line) and the original HB (red lines), we reconstruct the inner structure of the HB. It is clear that the HB is formed by exfoliating and lifting a certain thickness of MoS<sub>2</sub> surface layers. By statistical study of the HBs and comparing the depth of hexagonal pits and the bubble height, the typical thickness of the lifted MoS<sub>2</sub> is evaluated to range from 30 to 50 nm (40 to 60 layers).

#### 2.4. In Situ Tunneling Volt-Ampere Characteristics Between the MoS<sub>2</sub> Surface and the AFM Tip

The HBs are formed upon a positive bias, while the MoS<sub>2</sub> surface remains perfectly flat under negative bias. Control experiments are carried out with setting bias voltage as −10 V and +10 V, respectively. For each case, the voltage is switched on and off for

four cycles, and the in situ tunneling voltage-ampere characteristics is monitored. The voltage (red lines), tunneling currents  $I_T$  (orange lines) and deflection of the AFM tip (green lines) are plotted along the time line in Figure 4a,b. Positive tip deflection indicates the rising of the tip and thus the rising of the MoS<sub>2</sub> surface layers since the tip-surface distance ( $d_{TS}$ ) is kept constant.

As shown in Figure 4a, no tip deflection is observed during −10 V bias is on, meaning no HB formation. Meanwhile, we read a large current of −20 nA. It worth noting that ±20 nA is the maximum value of the amperemeter, so the actual value could be even greater. The negative sign of the current indicates that electrons are tunneling from sample to tip. As shown in the schematic drawing (Figure 4a, top panel), because the MoS<sub>2</sub> is *n*-type, excess electrons will accumulate on the surface under −10 V bias. Given the small tip-surface distance ( $d_{TS} = 20\text{--}40$  nm), intense tunneling electron flow appears, akin to thunder stroking on a lightning rod from cloud. This giant tunneling current equalizes the electric potentials between the tip and MoS<sub>2</sub> surface.

In stark contrast, the AFM tip rises by tens of nanometers during each cycle with a +10 V bias on, as shown in Figure 4b. The tunneling current from tip to sample  $I_T$  is small (≈2.9 nA) and discrete. The +10 V bias will first suck the resident electrons to the ground, and then electrically polarize the MoS<sub>2</sub> crystal in the out-of-plane direction. The electric potential difference between

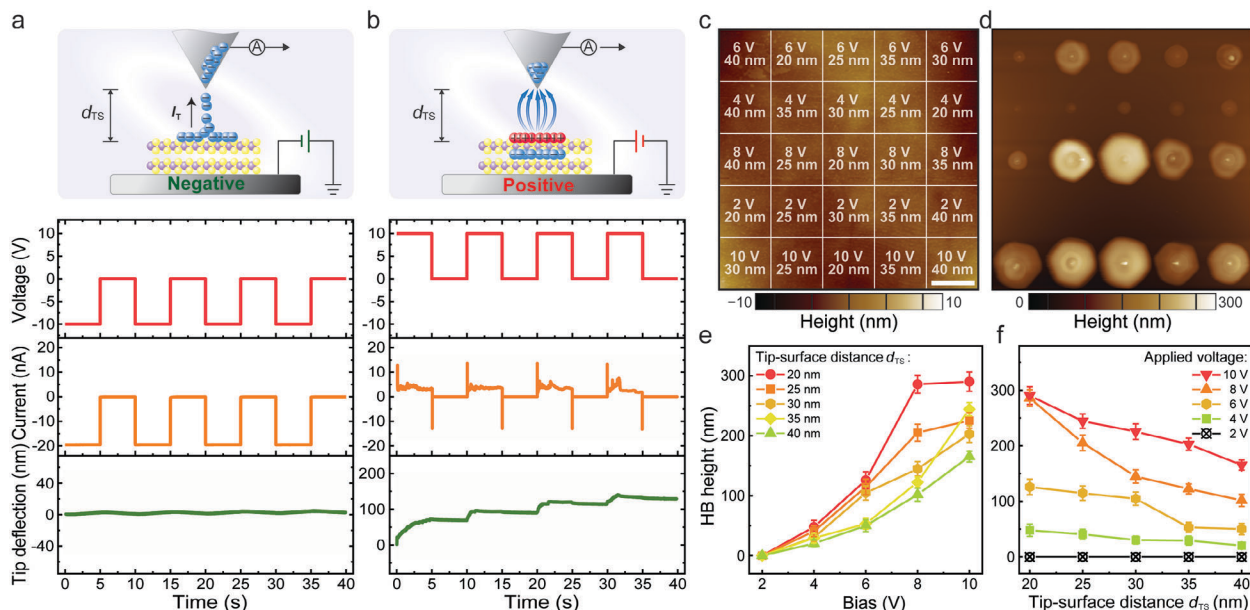


**Figure 4.** The controlled formation of HBs via varying the bias and tip-surface distance. The in situ monitoring of the tunneling volt-ampere characteristics when  $-10$  V (a) and  $+10$  V (b) biases are applied to the MoS<sub>2</sub> crystal, respectively. The upper panels of (a) and (b) are schematics of the local electrostatic conditions around the tip apex, where the blue and red spheres depict negative and positive charges, respectively. The lower panels of (a) and (b) show the in situ values of voltage, current, and deflection of the AFM tip along with time variation in red, orange, and green lines accordingly; The AFM topographies of a  $30 \times 30 \mu\text{m}^2$  area on the MoS<sub>2</sub> surface before (c) and after (d) the formation of HBs. The scale bar (white line in (c)) is  $5 \mu\text{m}$ . Each HB in (d) is formed with a specific combination of bias and tip-surface distance, which are labeled in (c) as a  $5 \times 5$  array; The dependence of HB height on (e) the bias voltage of the sample and (f) the set value of tip-surface distance.

the tip and sample surface will persist for long time, owing to the small tunneling current. Ideally, the Coulomb attractive force between the (negative and positive) charges at the tip ( $Q_T$ ) and the MoS<sub>2</sub> surface ( $Q_S$ ) can be evaluated using the Coulomb's law:  $F_C = k \frac{Q_T Q_S}{d_{TS}^2}$ , which will be greatly enhanced at small tip-surface distance. However, in reality the local charge density and distribution near the tip apex are complex functions of bias voltage, tunneling current, tip-surface configuration and time. To gain further insights on the effects of the Coulomb attractive force, we quantitatively monitor the HB size while varying the bias and tip-surface distance  $d_{TS}$ . Figure 4c and d are the topographies before and after the formation of HBs, the  $30 \times 30 \mu\text{m}^2$  area is divided into a  $5 \times 5$  grid with different bias and  $d_{TS}$  at each site (labeled in Figure 4c). The HBs won't form when bias is small (e.g.,  $\leq 2$  V) and/or  $d_{TS}$  is big (e.g.,  $\geq 50$  nm). As shown in Figure 4e,f, the height of HBs are positively and negatively correlated to the bias and  $d_{TS}$ , respectively. The results indicate that the size of the HBs can be controlled by varying the two parameters, which approximately follow the Coulomb's law.

### 3. Discussion

Our experimental results prove that the Coulomb attractive force is the main driving force of the HB formation. The adhesion energy ( $\gamma$ ) of the MoS<sub>2</sub>-MoS<sub>2</sub> interface is normally around  $30 \pm 16 \text{ meV}\text{\AA}^{-2}$ ,<sup>[47-49]</sup> therefore, the work done by the Coulomb attractive force induced by the tip needs to be sufficiently strong in order to initialize the exfoliation of the surface MoS<sub>2</sub> layers. In previous studies, similar surface bubbles generated by hydrogenation

inflating show dome-like shape, suggesting a homogeneous exfoliation.<sup>[49-52]</sup> In contrast, herein the tip-induced exfoliation develops radially from surface area proximate to the tip apex and shows a sixfold symmetry.

When the MoS<sub>2</sub> surface is lifted up, the tip-surface distance  $d_{TS}$  becomes smaller than the set point. The feedback loop of the AFM will raise the tip in order to restore to the set point. In this manner, the MoS<sub>2</sub> surface is continuously picked up. Judging from the structure of the HB and theoretical simulations, the formation process of a HB and its edge monolayers can be divided into three consecutive phases: Phase I – electrostatic mirroring the tip apex; Phase II – mechanical stretching; Phase III – strain releasing.

Phase I takes place immediately as the bias is applied. Initially the MoS<sub>2</sub> surface proximate to the tip apex will be subject to a Coulomb attractive force corresponding to the charge distribution that follows the cone shape of the tip apex, giving rise to a significant force over an area of the order of  $\text{nm}^2$ . Figure 5a simulates the distribution of electrostatic force on the sample surface (see details in Experimental Section and Section S4, Supporting Information). The 3D contour plots the force amplitude pointing upward, which is indeed mirroring the charge distribution of the tip apex. This specific force distribution will first lift up the surface layers at the center point. As the Coulomb force is inversely proportional to  $d_{TS}^2$ , moving away from the surface into the MoS<sub>2</sub> layers, there will eventually be a  $(n + 1)$ th layer of MoS<sub>2</sub> such that the Coulomb force is too weak to exfoliate. Therefore, the  $n$  layers of MoS<sub>2</sub> will be exfoliated and deformed into a cone, mirroring the shape of the tip apex.

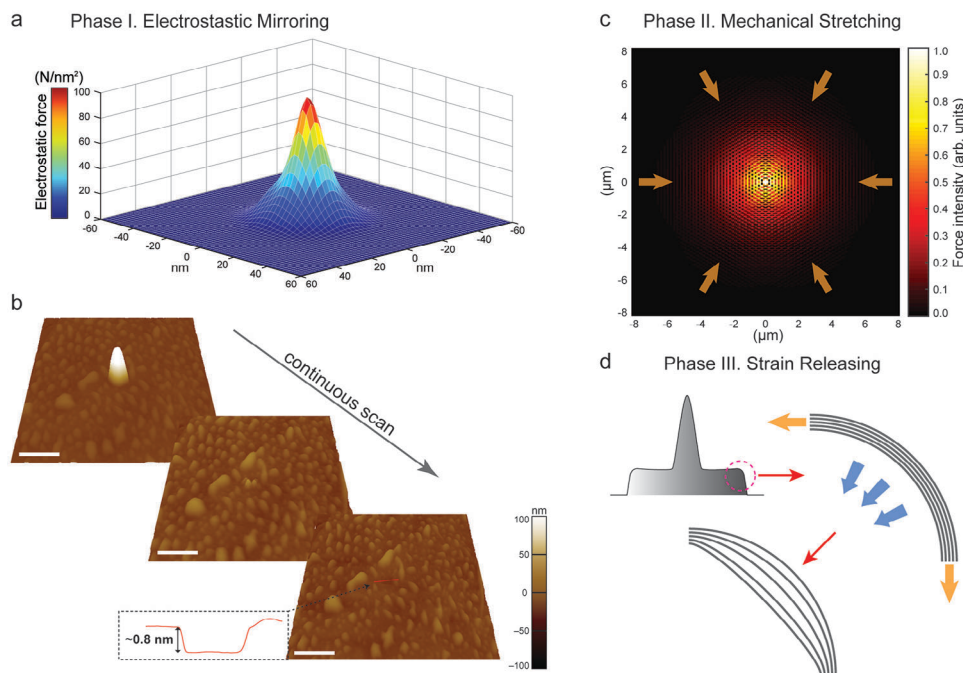


**Figure 5.** Three-phase formation of the hexagonal bubble and the edge monolayers. a) simulation of the distribution of electrostatic force on the surface of the MoS<sub>2</sub> crystal proximate to the conductive AFM tip apex, the force distribution mirrors the shape of the tip apex; b) the electrostatic force induced bubble on a monolayer MoS<sub>2</sub> on heavily doped Si substrate and its time evolution revealed by AFM topography (scale bar: 1 μm). The breakage of the monolayer bubble indicates that the monolayer was lifted up locally and experienced elastic deformation; c) in-plane stretch and the directional stress; d) self-exfoliation of the HB edge via strain releasing.

To verify this deformation of MoS<sub>2</sub> layers, a simplified test is carried out using a MoS<sub>2</sub> monolayer sample on a heavily doped silicon substrate. We set the tip to be at 30 nm to the monolayer and apply +4 V bias to the substrate for one cycle. The treated area is scanned in the tapping mode immediately. The images in Figure 5b show the topography evolution of the treated area. At first a cone structure mirroring the tip apex appears, which has the similar lateral size comparing to the cone of the HBs. The cone structure keeps collapsing as Coulomb attractive force is removed. Finally it disappears, leaving a small pit with ≈0.8 nm depth (see the inset section profile). It suggests that the monolayer cone is broken due to strain. Similar breakages are observed at the cone apex of HBs (Figure 1b,c). Based on these observations, the cone structure in monolayer and single crystal cases both are originated from the tip-like distribution of Coulomb attractive force.

Phase II starts when the cone structure stops “growing”, namely, the strain at the cone is equal to the Coulomb attractive force. At the moment, the coulomb attractive force on the outskirts MoS<sub>2</sub> surface is negligible, as it is about 150–200 nm (cone height) away from the tip apex. However, the strain from the cone, which is perpendicular to the MoS<sub>2</sub> surface will mechanically cleave off the *n* layers connected to it. The cleavage will propagate radially, until the exfoliated area (lateral size of HB) and interlayer adhesive force are big enough to pin it. Apparently, the cleavage propagation determines the lateral geometry of the bubble. We simulate the distribution of in-plane force on hexagonal lattice, with assuming a force pulling at a center point, as shown in Figure 5c. The force distribution presents a hexagonal pattern,

with the maximum force intensity along diagonals pointing to the center (see Section S4, Supporting Information). The simulation demonstrates that the hexagonal geometry of the HBs results from the hexagonal lattice of MoS<sub>2</sub>, which is consistent with our SHG results (Figure 2a–c). Besides, previous works also reported that the cleavage of TMDs layers usually favors specific edges along 60 or 120°.<sup>[53]</sup>

Phase III takes place when the bias is *off* and the Coulomb attractive force is withdrawn. The strain at the HBs will be completely released, as verified by our PL and SHG spectra with comparing to previous studies.<sup>[54–56]</sup> Due to the 2D nature, the MoS<sub>2</sub> layers can only be subject to in-plane strain.<sup>[54,55]</sup> Similarly, the releasing of the strain will be along the in-plane direction. Since the suspending layers at HB edge are anchored to both sides (Figure 5d), the two-side strain relief will merge and generate a resultant force along the out-of-plane direction, thus exfoliating the edge layers to multiple isolated monolayers. After Phase III, the formed HB area has no residual strain anymore, which can be confirmed by a Raman mapping across the HB (see Section S5 and Figure S9, Supporting Information). It is worth noting that the unique exfoliation may provide chances to obtain thick TMD film with monolayer-like properties, which is long desired but can not be made by stacking exfoliated monolayers due to inter-layer interactions.

## 4. Conclusion

In conclusion, we have achieved controllable exfoliation of the surface layers of MoS<sub>2</sub> single crystal to monolayers by

conductive AFM, through bias-enhanced Coulomb attractive force. The surface layers are exfoliated locally and shaped to micron-sized hexagonal bubbles, whose geometry orientation seamlessly matches and visualizes the hexagonal lattice of MoS<sub>2</sub>. The lateral edge of those hexagonal bubbles are composed of high-quality suspending monolayers, showing intense second harmonic generation and photoluminescence with subnanosecond excitonic lifetime and valley polarization. The Fermi energy of the MoS<sub>2</sub> layers within the hexagonal bubbles are modified toward *p*-type. By in situ monitoring of the tunneling volt-ampere characteristics and simulation of the force distribution, we illustrate the formation mechanism of those hexagonal bubbles. Our results provide a nontrivial way to obtain on-demand TMD monolayers of high crystalline quality and well-defined lattice orientation, which can be utilized to construct valleytronic and optoelectronic devices.

## 5. Experimental Section

**Sample Preparation:** Single crystal MoS<sub>2</sub> was grown by chemical vapor transport reactions in sealed quartz ampules. Molybdenum, sulfur, and iodine (transport agent) were loaded in stoichiometric ratio. The sealed ampules were put in two-zone tube furnaces, with setting the precursor and growth ends at 950 and 900 °C, respectively. After two weeks, the ampules were opened and centimeter sized crystal flakes were harvested. The crystal flakes were pasted onto the iron disk using conductive silver paint (Ted Pella, Inc.). Mono- to few-layer MoS<sub>2</sub> micro sheets were prepared by scotch tape exfoliation, and dry transferred to heavily doped silicon substrate.

**AFM Operations:** Iron disk carrying single crystal MoS<sub>2</sub> was mounted to AFM sample stage (Cypher ES, Asylum Research), and wired to the bias functional generator that was integrated within the AFM system. The AFM conductive tips were used for SKPM and bubble generation (NSC18/Pt with a nominal spring constant of 2.8 Nm<sup>-1</sup>). Positive or negative bias (maximum 10 V) were applied to the sample (for comparison), while the tip apex was lifted at a certain height above the sample surface. The topography images were taken in tapping mode. To remove the pop-up body of the hexagonal bubbles, contact mode was used to scan the region of interest with the feedback loop is off. A stiff cantilever (NSC15/Al) with a nominal spring constant of 40 Nm<sup>-1</sup> was used for tapping/contact mode AFM.

**Optical Spectroscopic Measurements:** For the fluorescence microscopic measurement, blue light was shined on the MoS<sub>2</sub> surface for excitation and the reflected signals were cut off using a long-wavelength-pass filter and collected by a digital camera. Raman and PL spectra were taken on the MoS<sub>2</sub> surface in back-scattering geometry using the Horiba LabRam system with 532 nm laser excitation. The 2D spatial mapping of spectra was realized by using a scanning Galvo mirror system to tilt the light beam. The time-resolved PL was measured with a femtosecond pulsed laser (400 nm, 80MHz) and detected using a single photon detector connected to a time-correlated single photon counting system.

**Theoretical Simulations:** In order to gain insight on the “pulling” (Coulomb attractive force) that the AFM tip is exerting on the MoS<sub>2</sub> surface, we simulate the distribution of charge density on the MoS<sub>2</sub> surface proximate to the tip apex. In light of the experiment configuration, a random distribution of free point charges – electrons – at the tip apex was assumed, taking into consideration the tip radius of 20 nm. The point charges were fixed at a distance of  $d = 20$  nm as exemplified in the experiments. The surface charge density induced by each point charge was calculated using the method of image charges.<sup>[57]</sup> Following the Coulomb attractive force between the tip apex and sample surface, the distribution of in-plane force was simulated on a 2D hexagon grid as in the lattice arrangement of the MoS<sub>2</sub>. Assuming a force pulling at a point on the grid, the in-plane forces directed toward the point was resolved on the “bonds” between points on the hexagonal grid. More details of the

calculations and simulations can be found in Section S4 (Supporting Information).

## Supporting Information

Supporting Information is available from the Wiley Online Library or from the author.

## Acknowledgements

H.A. thanks the funding support of the Australian Research Council through the ARC Future Fellowship (FT180100361). X. L. acknowledged the support from Center of Free Electron Laser & High Magnetic Field at Anhui University. This work was, in part, supported by a JST-CREST project (JPM)CR16F2) and a JSPS Grants-in-Aid for Scientific Research (A) (21H04652).

## Conflict of Interest

The authors declare no conflict of interest.

## Author Contributions

S.L. and H.A. conceived the initial idea for this research. S.L. and H.A. carried out the sample preparation and AFM experiments. S.L. performed the optical spectroscopic measurements. C.F. carried out the theoretical simulation. S.L. analyzed the data and wrote the manuscript with input from all the authors. X.L., B.H.T., Q.Z., and N.T.N. revised the manuscript. H.A. supervised the whole project.

## Data Availability Statement

The data that support the findings of this study are available from the corresponding author upon reasonable request.

## Keywords

2D semiconductor, conductive AFM, Coulomb Force, monolayers, optical properties

Received: July 6, 2023  
Revised: September 22, 2023  
Published online:

- [1] A. Splendiani, L. Sun, Y. Zhang, T. Li, J. Kim, C.-Y. Chim, G. Galli, F. Wang, *Nano Lett.* **2010**, *10*, 1271.
- [2] K. F. Mak, C. Lee, J. Hone, J. Shan, T. F. Heinz, *Phys. Rev. Lett.* **2010**, *105*, 136805.
- [3] A. Chernikov, T. C. Berkelbach, H. M. Hill, A. Rigosi, Y. Li, O. B. Aslan, D. R. Reichman, M. S. Hybertsen, T. F. Heinz, *Phys. Rev. Lett.* **2014**, *113*, 076802.
- [4] K. He, N. Kumar, L. Zhao, Z. Wang, K. F. Mak, H. Zhao, J. Shan, *Phys. Rev. Lett.* **2014**, *113*, 026803.
- [5] M. M. Ugeda, A. J. Bradley, S.-F. Shi, H. Felipe, Y. Zhang, D. Y. Qiu, W. Ruan, S.-K. Mo, Z. Hussain, Z.-X. Shen, F. Wang, S. G. Louie, M. F. Crommie, *Nat. Mater.* **2014**, *13*, 1091.

- [6] A. Granados del Aguila, S. Liu, T. T. H. Do, Z. Lai, T. H. Tran, S. R. Krupp, Z.-R. Gong, H. Zhang, W. Yao, Q. Xiong, *ACS Nano* **2019**, *13*, 13006.
- [7] Y. Li, Y. Rao, K. F. Mak, Y. You, S. Wang, C. R. Dean, T. F. Heinz, *Nano Lett.* **2013**, *13*, 3329.
- [8] K. L. Seyler, J. R. Schaibley, P. Gong, P. Rivera, A. M. Jones, S. Wu, J. Yan, D. G. Mandrus, W. Yao, X. Xu, *Nat. Nanotechnol.* **2015**, *10*, 407.
- [9] A. Han, A. Aljarb, S. Liu, P. Li, C. Ma, F. Xue, S. Lopatin, C.-W. Yang, J.-K. Huang, Y. Wan, X. Zhang, Q. Xiong, K.-W. Huang, V. Tung, T. D. Anthopoulos, L.-J. Li, *Nanoscale Horiz.* **2019**, *4*, 1434.
- [10] K. F. Mak, K. He, J. Shan, T. F. Heinz, *Nat. Nanotechnol.* **2012**, *7*, 494.
- [11] H. Zeng, J. Dai, W. Yao, D. Xiao, X. Cui, *Nat. Nanotechnol.* **2012**, *7*, 490.
- [12] S. Liu, A. Granados del Aguila, X. Liu, Y. Zhu, Y. Han, A. Chaturvedi, P. Gong, H. Yu, H. Zhang, W. Yao, Q. Xiong, *ACS Nano* **2020**, *14*, 9873.
- [13] S. Liu, Y. Wu, X. Liu, A. G. del Aguila, F. Xuan, A. Chaturvedi, H. Zhang, S. Y. Quek, Q. Xiong, *Sci. China Mater.* **2021**, *64*, 2507.
- [14] K. Tran, G. Moody, F. Wu, X. Lu, J. Choi, K. Kim, A. Rai, D. A. Sanchez, J. Quan, A. Singh, J. Embley, A. Zepeda, M. Campbell, T. Autry, T. Taniguchi, K. Watanabe, N. Lu, S. K. Banerjee, K. L. Silverman, S. Kim, E. Tutuc, L. Yang, A. H. MacDonald, X. Li, *Nature* **2019**, *567*, 71.
- [15] X. Liu, J. Pei, Z. Hu, W. Zhao, S. Liu, M.-R. Amara, K. Watanabe, T. Taniguchi, H. Zhang, Q. Xiong, *Nano Lett.* **2020**, *20*, 5359.
- [16] E. Marcellina, X. Liu, Z. Hu, A. Fieramosca, Y. Huang, W. Du, S. Liu, J. Zhao, K. Watanabe, T. Taniguchi, Q. Xiong, *Nano Lett.* **2021**, *21*, 4461.
- [17] K. Shinokita, X. Wang, Y. Miyauchi, K. Watanabe, T. Taniguchi, K. Matsuda, *Adv. Funct. Mater.* **2019**, *29*, 1900260.
- [18] S. Feng, C. Cong, S. Konabe, J. Zhang, J. Shang, Y. Chen, C. Zou, B. Cao, L. Wu, N. Peimyoo, B. Zhang, T. Yu, *Small* **2019**, *15*, 1805503.
- [19] F. Ohnesorge, G. Binnig, *Science* **1993**, *260*, 1451.
- [20] F. J. Giessibl, *Rev. Mod. Phys.* **2003**, *75*, 949.
- [21] T. Namazu, Y. Isono, T. Tanaka, *J. Microelectromech. Syst.* **2000**, *9*, 450.
- [22] Y. Sugimoto, M. Abe, S. Hirayama, N. Oyabu, O. Custance, S. Morita, *Nat. Mater.* **2005**, *4*, 156.
- [23] Y. Sugimoto, P. Pou, O. Custance, P. Jelinek, M. Abe, R. Perez, S. Morita, *Science* **2008**, *322*, 413.
- [24] O. Custance, R. Perez, S. Morita, *Nat. Nanotechnol.* **2009**, *4*, 803.
- [25] N. Pavliček, L. Gross, *Nat. Rev. Chem.* **2017**, *1*, 1.
- [26] T. Junno, K. Deppert, L. Montelius, L. Samuelson, *Appl. Phys. Lett.* **1995**, *66*, 3627.
- [27] P. Mesquida, A. Stemmer, *Adv. Mater.* **2001**, *13*, 1395.
- [28] J. Xu, K. J. Kwak, J. L. Lee, G. Agarwal, *Small* **2010**, *6*, 2105.
- [29] Y. Huang, Y.-H. Pan, R. Yang, L.-H. Bao, L. Meng, H.-L. Luo, Y.-Q. Cai, G.-D. Liu, W.-J. Zhao, Z. Zhou, L.-M. Wu, Z.-L. Zhu, M. Huang, L.-W. Liu, L. Liu, P. Cheng, K.-H. Wu, S.-B. Tian, C.-Z. Gu, Y.-G. Shi, Y.-F. Guo, Z. G. Cheng, J.-P. Hu, L. Zhao, G.-H. Yang, E. Sutter, P. Sutter, Y.-L. Wang, W. Ji, X.-J. Zhou, et al., *Nat. Commun.* **2020**, *11*, 2453.
- [30] F. Liu, W. Wu, Y. Bai, S. H. Chae, Q. Li, J. Wang, J. Hone, X.-Y. Zhu, *Science* **2020**, *367*, 903.
- [31] A. C. Johnston, S. I. Khondaker, *Adv. Mater. Interfaces* **2022**, *9*, 2200106.
- [32] C. Chen, A. R. B. de Castro, Y. Shen, *Phys. Rev. Lett.* **1981**, *46*, 145.
- [33] Y. Shen, *Annu. Rev. Phys. Chem.* **1989**, *40*, 327.
- [34] R. Suzuki, M. Sakano, Y. Zhang, R. Akashi, D. Morikawa, A. Harasawa, K. Yaji, K. Kuroda, K. Miyamoto, T. Okuda, K. Ishizaka, R. Arita, Y. Iwasa, *Nat. Nanotechnol.* **2014**, *9*, 611.
- [35] L. M. Malard, T. V. Alencar, A. P. M. Barboza, K. F. Mak, A. M. De Paula, *Phys. Rev. B* **2013**, *87*, 201401.
- [36] M. Zhao, Z. Ye, R. Suzuki, Y. Ye, H. Zhu, J. Xiao, Y. Wang, Y. Iwasa, X. Zhang, *Light Sci. Appl.* **2016**, *5*, e16131.
- [37] M. Palumbo, M. Bernardi, J. C. Grossman, *Nano Lett.* **2015**, *15*, 2794.
- [38] M. Selig, G. Berghäuser, A. Raja, P. Nagler, C. Schüller, T. F. Heinz, T. Korn, A. Chernikov, E. Malic, A. Knorr, *Nat. Commun.* **2016**, *7*, 1.
- [39] H. Nan, Z. Wang, W. Wang, Z. Liang, Y. Lu, Q. Chen, D. He, P. Tan, F. Miao, X. Wang, J. Wang, Z. Ni, *ACS Nano* **2014**, *8*, 5738.
- [40] M. Amani, D.-H. Lien, D. Kiriya, J. Xiao, A. Azcatl, J. Noh, S. R. Madhupathy, R. Addou, S. Kc, M. Dubey, K. Cho, R. M. Wallace, S.-C. Lee, J.-H. He, J. W. Ager, X. Zhang, E. Yablonovitch, A. Javey, *Science* **2015**, *350*, 1065.
- [41] B. Radisavljevic, M. B. Whitwick, A. Kis, *ACS Nano* **2011**, *5*, 9934.
- [42] K. F. Mak, K. He, C. Lee, G. H. Lee, J. Hone, T. F. Heinz, J. Shan, *Nat. Nanotechnol.* **2011**, *6*, 146.
- [43] A. Chernikov, A. M. van der Zande, H. M. Hill, A. F. Rigosi, A. Velauthapillai, J. Hone, T. F. Heinz, *Phys. Rev. Lett.* **2015**, *115*, 126802.
- [44] A. Castellanos-Gomez, E. Cappelluti, R. Roldán, N. Agrait, F. Guinea, G. Rubio-Bollinger, *Adv. Mater.* **2013**, *25*, 899.
- [45] S. Choi, Z. Shaolin, W. Yang, *J. Korean Phys. Soc.* **2014**, *64*, 1550.
- [46] F. Giannazzo, G. Fischella, A. Piazza, S. Agnello, F. Roccaforte, *Phys. Rev. B* **2015**, *92*, 081307.
- [47] G. Levita, E. Molinari, T. Polcar, M. C. Righi, *Phys. Rev. B* **2015**, *92*, 085434.
- [48] E. Blundo, T. Yildirim, G. Pettinari, A. Polimeni, *Phys. Rev. Lett.* **2021**, *127*, 046101.
- [49] C. Di Giorgio, E. Blundo, G. Pettinari, M. Felici, Y. Lu, A. M. Cucolo, A. Polimeni, F. Bobba, *Adv. Mater. Interfaces* **2020**, *7*, 2001024.
- [50] H. An, J. G. S. Moo, B. H. Tan, S. Liu, M. Pumera, C.-D. Ohl, *Carbon* **2017**, *123*, 84.
- [51] Z. Dai, Y. Hou, D. A. Sanchez, G. Wang, C. J. Brennan, Z. Zhang, L. Liu, N. Lu, *Phys. Rev. Lett.* **2018**, *121*, 266101.
- [52] B. H. Tan, J. Zhang, J. Jin, C. H. Ooi, Y. He, R. Zhou, K. Ostrikov, N.-T. Nguyen, H. An, *Nano Lett.* **2020**, *20*, 3478.
- [53] Y. Guo, C. Liu, Q. Yin, C. Wei, S. Lin, T. B. Hoffman, Y. Zhao, J. Edgar, Q. Chen, S. P. Lau, J. Dai, H. Yao, H.-S. P. Wong, Y. Chai, *ACS Nano* **2016**, *10*, 8980.
- [54] K. He, C. Poole, K. F. Mak, J. Shan, *Nano Lett.* **2013**, *13*, 2931.
- [55] H. J. Conley, B. Wang, J. I. Ziegler, R. F. Haglund Jr, S. T. Pantelides, K. I. Bolotin, *Nano Lett.* **2013**, *13*, 3626.
- [56] L. Mennel, M. M. Furchi, S. Wachter, M. Paur, D. K. Polyushkin, T. Mueller, *Nat. Commun.* **2018**, *9*, 1.
- [57] D. J. Griffiths, Introduction to electrodynamics, 3rd ed. Prentice-Hall Inc, New Jer, **1999**, p 127.